AAAS
Research
Volume 2022, Article ID 9820585, 12 pages
https://doi.org/10.34133/2022/9820585

Research Article

Cross-Scale Synthesis of Organic High-*k* Semiconductors Based on Spiro-Gridized Nanopolymers

Dongqing Lin,[1] Wenhua Zhang,[2] Hang Yin,[3] Haixia Hu,[3] Yang Li,[1] He Zhang,[1] Le Wang,[1] Xinmiao Xie,[1,4] Hongkai Hu,[1] Yongxia Yan,[1] Haifeng Ling,[1] Jin'an Liu,[1] Yue Qian,[1] Lei Tang,[1] Yongxia Wang,[1] Chaoyang Dong,[1] Linghai Xie,[1,5] Hao Zhang,[6] Shasha Wang,[1] Ying Wei,[1] Xuefeng Guo,[4] Dan Lu,[6] and Wei Huang[1,5]

[1]*Centre for Molecular Systems and Organic Devices (CMSOD), State Key Laboratory of Organic Electronics and Information Displays & Institute of Advanced Materials (IAM), Nanjing University of Posts & Telecommunications, 9 Wenyuan Road, Nanjing 210023, China*
[2]*National Synchrotron Radiation Laboratory, Anhui Provincial Engineering Laboratory of Advanced Functional Polymer Film, CAS Key Laboratory of Soft Matter Chemistry, University of Science and Technology of China, Hefei 230026, China*
[3]*School of Physics, State Key Laboratory of Crystal Materials, Shandong University, Jinan, Shandong 250100, China*
[4]*Beijing National Laboratory for Molecular Sciences, National Biomedical Imaging Center, College of Chemistry and Molecular Engineering, Peking University, Beijing 100871, China*
[5]*Frontiers Science Center for Flexible Electronics (FSCFE), MIIT Key Laboratory of Flexible Electronics (KLoFE), Northwestern Polytechnical University, Xi'an 710072, China*
[6]*State Key Laboratory of Supramolecular Structure and Materials, College of Chemistry, Jilin University, 2699 Qianjin Avenue, Changchun 130012, China*

Correspondence should be addressed to Linghai Xie; iamlhxie@njupt.edu.cn, Ying Wei; iamywei@njupt.edu.cn, and Wei Huang; iamdirector@fudan.edu.cn

Received 31 August 2021; Accepted 6 December 2021; Published 12 January 2022

High dielectric constants in organic semiconductors have been identified as a central challenge for the improvement in not only piezoelectric, pyroelectric, and ferroelectric effects but also photoelectric conversion efficiency in OPVs, carrier mobility in OFETs, and charge density in charge-trapping memories. Herein, we report an ultralong persistence length ($l_p \approx 41$ nm) effect of spiro-fused organic nanopolymers on dielectric properties, together with excitonic and charge carrier behaviors. The state-of-the-art nanopolymers, namely, nanopolyspirogrids (NPSGs), are synthesized via the simple cross-scale Friedel-Crafts polygridization of A_2B_2-type nanomonomers. The high dielectric constant ($k = 8.43$) of NPSG is firstly achieved by locking spiro-polygridization effect that results in the enhancement of dipole polarization. When doping into a polystyrene-based dielectric layer, such a high-*k* feature of NPSG increases the field-effect carrier mobility from 0.20 to 0.90 $\text{cm}^2\ \text{V}^{-1}\ \text{s}^{-1}$ in pentacene OFET devices. Meanwhile, amorphous NPSG film exhibits an ultralow energy disorder (<50 meV) for an excellent zero-field hole mobility of $3.94 \times 10^{-3}\ \text{cm}^2\ \text{V}^{-1}\ \text{s}^{-1}$, surpassing most of the amorphous π-conjugated polymers. Organic nanopolymers with high dielectric constants open a new way to break through the bottleneck of efficiency and multifunctionality in the blueprint of the fourth-generation semiconductors.

1. Introduction

The fourth-generation semiconductors have been conceived as the cornerstone of intelligent flexible electronics, which would revolute the function and morphology of integrated circuits beyond Moore's law [1, 2]. In this aspect, organic semiconductors [3] hold promising advantages over atomically precise synthesis, structural diversity, multifunctional integration, and high biocompatibility, in promising applications of large-area, ultrathin, and wearable optoelectronic devices. However, even achieving significant development in organic light-emitting diodes [*4*], solar cells [*5*], and transistors [*6*, *7*], organic semiconductors still suffer from low device performances, versus the rising hybrid perovskites [*8*] and inorganic counterparts. One of the fundamental origins for the dilemma situation is molecular nanoscale limitation that results in insufficient charge-screening behaviors and low dielectric constants ($k = 2 \sim 4$) [*9*]. Actually, dielectric constant is directly related to not only piezoelectric, pyroelectric, or ferroelectric effects [*10*] but also optoelectronic performances including charge separation efficiency in OPVs [*11*], carrier mobility in OFETs [*12*], and charge density in charge-trapping memories [*13*]. Particularly, high dielectric constant $k \geq 10$ is a prerequisite of band-like carrier transport [*14*] and Wannier-Mott-like excitons [*15*] for high-performance inorganic semiconductors. However, it is quite difficult to improve k values only through carbon element, because the small electronic cloud volume leads to an intrinsically low polarization efficiency [*16*]. In consideration of carbon nanostructures [*17–19*] that play a key role in wave absorption materials with excellent dielectric properties, we design organic nanopolymers to propagate dipole polarization through effectively overcoming the limitation of molecular nanoscale.

Cross-scale polygridization is a chemical platform to transform π-functional backbones into covalently ordered nanoarchitectures (with sizes of 10~100 nm) with promising applications in nanoelectronics and plastic electronics [*17*, *20*], based on the extensibility and scalability of molecular nanogrid vertexes [*2*]. Generally, gridarene-based organic nanopolymers (also called polygrids) are one-dimensional covalent nanochains with intermediate main-chain rigidity between π-conjugated polymers and carbon nanotubes (CNT). However, these single-bond-linked polygrids [*21*] with relatively large conformational entropy exhibit a limited persistence length ($l_p \approx 16$ nm) and thus disfavor covalent nanoscale ordering. Rhombus-type polygrids (RPGs), with backbone shapes resembling macroscopically expandable coat and cap racks (Figure 1(a)), offer an alternative installing paradigm to covalently lock conformational rotation and increase single-chain rigidity. In order to create double-stranded RPGs, we introduce orthogonal spiroaromatic building blocks as diagonal vertexes of rhombus-type nanogrid (RGs) to construct spiro-nanopolymers. Figure 1(b) exhibits the structure of target nanopolyspirogrids (NPSGs) with blue-emitting terfluorenyl moieties linked by 3,3-dithiophenyl transverse beams at the spirosites (Figure 1(c)). Particularly, the dithiophenyl group ensures regular and high-efficient covalent linkages during Friedel-Crafts processes [*22*]. Herein, we synthesize spirodithiophenefluorene- (SDTF-) based spirodigrids (SDGs) and one-dimensional NPSGs with a length × width × height scale of $2 \sim 50 \times 2 \times 2.5 \sim 3.5\,\mathrm{nm}^3$, via the kinetically controlled spiro-polygridization of A_2B_2-type nanosynthons. An ultralong $l_p = 41$ nm is demonstrated by synchrotron radiation small-angle X-ray (SAXS) and static light scattering (SLS). Even with π-interrupted backbone, such ultrarigid NPSG exhibits a high dielectric constant ($k = 8.43$), an ultralow energy disorder ($\sigma = 46.6$ meV), and a highest carrier mobility ($\mu = 3.94 \times 10^3\,\mathrm{cm^2\,V^{-1}\,s^{-1}}$) in amorphous states, suggesting excellent electrical properties beyond π-conjugated polymers.

2. Results and Discussion

2.1. Synthesis and Characterizations of NPSG Nanochains. NPSGs can be synthesized via the Friedel-Crafts polygridization of SDTF-based terfluorenyl diol (STF-DOH), as one of A_2B_2-type nanosynthons (Figure 2(a)). Such nanosynthon consists of a 3,3-bithiophene-type benzenoid group (as B_2-part) at the middle and two tertiary alcohols (as A_2-part) at the ends, which enables the geometric matching between reactive 2-sites of thiophenes and 9-sites of fluorene-based carbocationic species for the formation of C-C bonds (Figure S9). As the fluorenol chirality does not influence the gridization/polygridization pathways due to S_{N2}-type process [*23*], we performed the polygridization of STF-DOH in a chirality-mixed manner (mixed with *rac* and *meso*-configurations). In Figure 2(a), under the condition of $BF_3{\bullet}OEt_2$ (as acid catalyst [*24*]) in 1,2-dichloroethane (DCE) solvent and the dilute STF-DOH concentration ($C_{\text{STF-DOH}} = 2$ mM), the linear soluble NPSG were afforded in ~60% yield. Further, elongating the reaction time from 0.5 min to 4~8 h increases the number-average degree of polymerization (DP_n) of NPSG from 5.2 to 26.1 (Figure S10), corresponding to the average contour length (l_c) of 25~30 nm. However, the longer polygridization time (13~22 h) results in the formation of hyperbranched polygrids (HBPGs), suggesting that the spiro-polygridization into NPSG should be in kinetic control. In addition, under the same polygridization time (4 h), increasing $C_{\text{STF-DOH}}$ to 6 mM can generate longer NPSG nanochains with $l_c \approx 58$ nm, corresponding to the weight-average degree of polymerization (DP_w) of ~65 (Figure S12). Nevertheless, higher $C_{\text{STF-DOH}}$ (12~16 mM) affords insoluble cross-linked polymers (CLP) in ~90% yield, whereas NPSG nanochains were not obtained.

The NPSG structures with $l_c \approx 2 \sim 50$ nm were characterized by nuclear magnetic resonance (NMR), Fourier transform infrared (FT-IR), and Mass Spectrometry (MS). The MS characterization shows $m/z = 2437.32$ for SDG and $m/z = 3497.45$ for spirotrigrid (DP = 3 of NPSG), both of which are consistent with individual formula and isotopic distributions (Figure S29). Moreover, the oligomers with higher DP were also detected (Figure S32), including $m/z = 4557.19$ for DP = 4, $m/z = 5618.55$ for DP = 5, and $m/z = 6679.29$ for DP = 6, respectively, where each molecular weight difference between adjacent DP values ($m/z \approx 1060$) is consistent with the structural feature. Through ^{13}C NMR spectra (Figure S33), the absence of carbon signals at 54 ppm (the 9-position of phenylfluorenes) and 83.4 ppm (the 9-position of fluorenols) supports the occurrence of polygridization and the termination with A_1B_1 synthons, which eliminate hydroxyl groups at chain-ends (also confirmed by FT-IR spectra in Figure S34).

Further, the linear main-chain configuration of NPSG nanochains was demonstrated by gel permeation chromatography (GPC), dynamic light scattering (DLS), and SAXS.

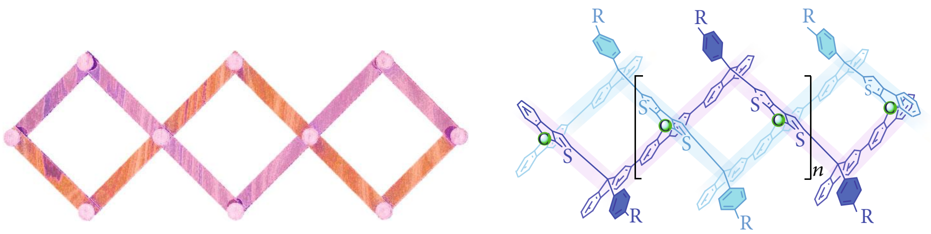

Expandable wooden hanging rack

(a)

Nanopolyspirogrids (NPSGs)

(b)

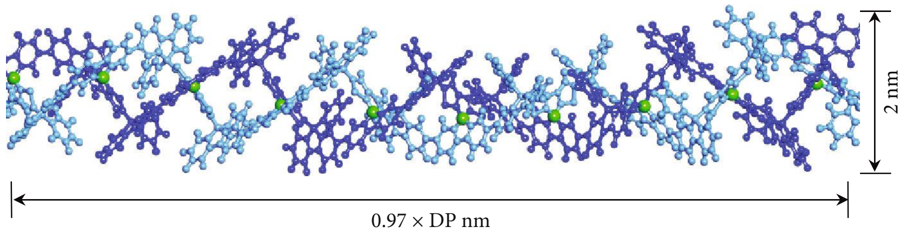

(c)

Figure 1: Nanopolyspirogrid (NPSG) models. (a) The wooden structure in an expandable hanging rack. (b, c) Molecular structures and 3D atomistic models of NPSG, respectively.

Through the analysis of GPC spectra (Figure 2(b)), the Mark-Houwink exponent (α) of NPSG oligomers (DP = 2 ~ 5) was calculated to be 1.175, which falls into the range of rod-like conformation [25] ($\alpha = 1.0 \sim 1.7$) rather than branched configurations ($\alpha = 0.3 \sim 0.8$) [26] (Figure S35). Meanwhile, through DLS characterization, the relationship of hydrodynamic radius ($R_h = 7.6 \sim 14.7$ nm) in $R_h \sim \mathrm{DP}_w{}^{0.99}$ also reveals the rod-like conformation of NPSG nanochains, consistent with the visualization of atomic force microscopy (Figure S37). Via SAXS characterization, the rod-like conformation of NPSG nanochains is firmly confirmed by the absence of intrachain folding (deduced from Kratky plots q^2I in Figure S38) and the ultralow mass fractal dimension (d) in scattering laws $I \sim q^{-0.8 \sim -0.55}$ (Figure 2(c)), where I and q are scattering intensity and vector, respectively. In contrast, the byproduct HBPG shows a high $d = 3.18$ with the presence of intrachain folding (Figure S38), as in agreement with spherical branching backbones ($d \approx 2 \sim 3$) [27]. These results rule out the probability of branched structures (with significant amount) on NPSG nanochains. Deeply, the distance distribution function $P(r)$ of NPSG (Figure S40) with a series of peaks at $r = 2$, 7.5, 12.5, and 18 nm suggests the covalently ordered periodic distribution on polygrid segments, unlike only a broad Gaussian-like pattern on random coil-like backbones [28].

The rigidity of NPSG nanochains was investigated via SLS and SAXS characterizations, as well as molecular dynamic simulations. We obtained the radius of gyration (R_g) of 28.5 ~ 31.1 nm for the synthesized NPSG with $l_c = 26 \sim 30$ nm (Figure 2(d)), probably indicating $l_p \geq 30$ nm. For longer NPSG nanochains with $l_c \approx 58$ nm, we obtained $R_g = 53.2$ nm from SLS results and $R_g = 50.8$ nm from SAXS data (Figure S44). Based on the rigidity calculation [29], the average $R_g = 52$ nm and $l_c = 58$ nm afford $l_p \approx 41$ nm, as beyond all soluble π-conjugated polymers [29, 30] ($l_p = 3 \sim 20$ nm, Figure S46). These results confirm the ultralong l_p property arising from synergistically double-bond-linked polygridization effects, as similar to DNA systems ($l_p = 53$ nm for double-stranded backbones and $l_p = 1.5$ nm for single-stranded main-chains) [31]. Further, through molecular dynamic simulation (Figure S47-S55), we evaluated l_p of all NPSG backbones (in an approximate Θ state, Figure 2(e)), including interlaced configurations ($l_p = 155.8$, 43.7, 62.5, and 100 nm for *SS*-isotacticity, *SR*-isotacticity, *SS-SR*-syndiotacticity, and *SS-RR*-syndiotacticity, respectively) and uninterlaced counterparts ($l_p = 34.5 \sim 47.6$ nm). The above l_p values are 1.8~27 times higher than that of single-bond-linked polygrids (SBPG) with $l_p = 5.7 \sim 19.4$ nm, revealing the effect of double-bond-linked spiro-polygridization on restricting conformational rotations of RG units (Figure S50). Further, l_p of NPSGs are 11~53 times longer than that of single-stranded π-interrupted polymers (SSIP) with $l_p = 3.7$ nm. In addition, the incorporation of ungridized structural defects also diminishes l_p to 5~10 nm (Figure S58-60), which reconfirms that our synthesized NPSG nanochains should have few ungridized structural defects. It is noted that such ultrarigid NPSG nanochains provide a unique molecular platform for covalent nanoscale ordering.

2.2. Dielectric Properties and Dipole Polarization of NPSG.

We probed the dramatic spiro-polygridization effect on the dielectric constant (k) at the frequency scope of $10^3 \sim 10^5$ Hz (Figure 3(a)), through an impedance analyzer. In Figure 3(a), NPSG has an obviously higher $k \approx 8.43$ than that of single-bond-linked polygrid PG-Cz ($k \approx 3.82$) [32], as well as π-conjugated polythiophenes ($k \approx 3.75$) [9] and

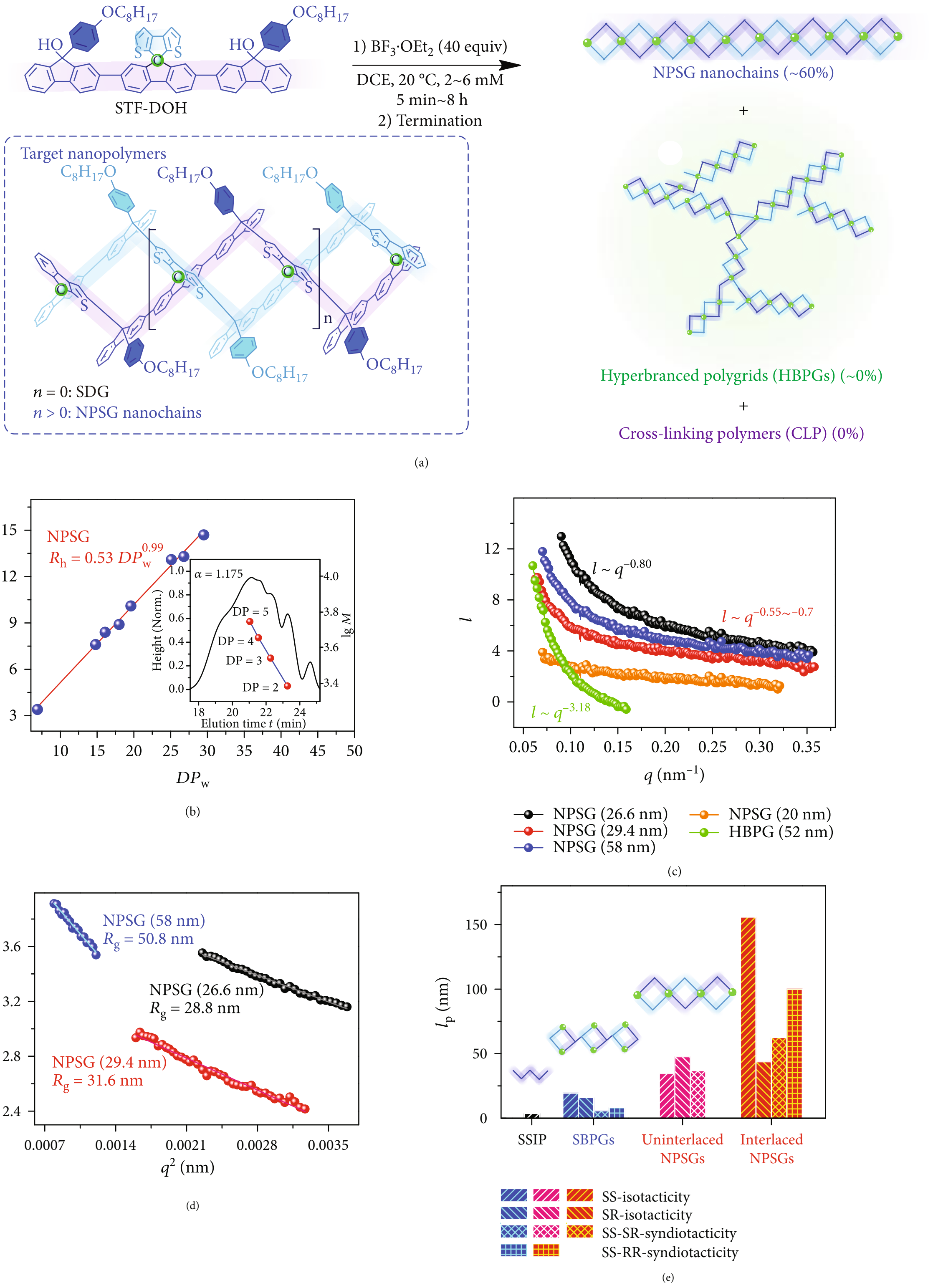

Figure 2: Synthesis and characterizations of NPSG. (a) Chemical equation of polygridization reaction. The likely structure of hyperbranched polygrid (HBPG), as byproducts, is provided in Figure S11. (b) The hydrodynamic radius (R_h) relying on DP_w. The calibration of NPSG oligomers (with the degree of polymerization DP = 2 ~ 5) from GPC spectra was also provided to calculate the Mark-Houwink exponent (α). (c) The scaling plots $I \sim q^{-d}$ of NPSG and HBPG. The l_c of NPSG (in the brackets) are transformed from individual R_h or DP_w values. (d) The Quinier plots of NPSG with various l_c (in the brackets). The calculated radius of gyration (R_g) is also provided. (e) The simulation of l_p of SSIP (orange), SBPGs (deep blue), and NPSGs (pink and red). The SSIP chain is defined as the single-chain segment of NPSG that removes all spiro-carbon atoms.

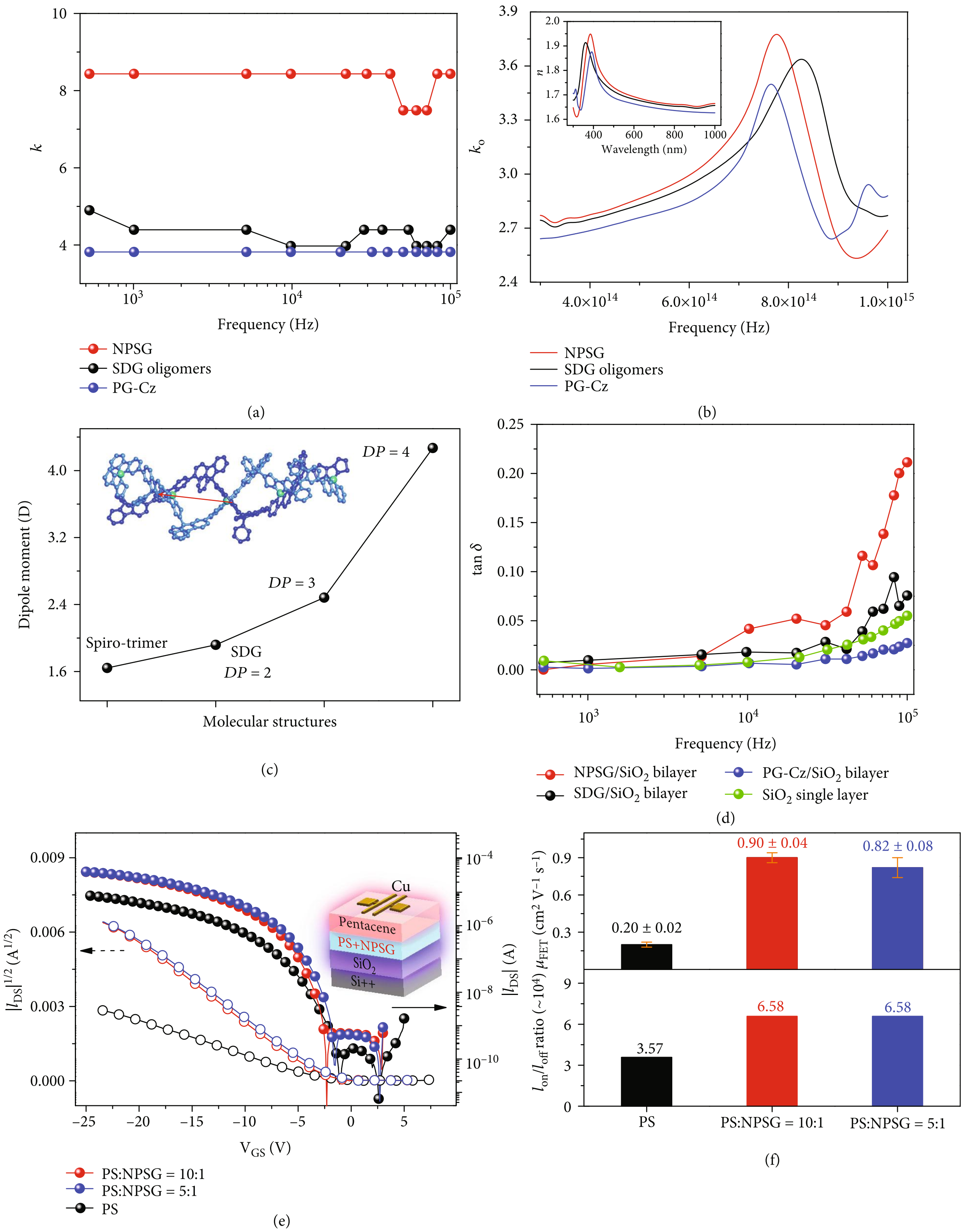

FIGURE 3: Dielectric features and OFET application of NPSG. (a) The dielectric constant (k) in the frequency range of 500~10^5 Hz. (b) The optical dielectric constant (k_o) and refractive index (n) of NPSG and other nanopolymer films. (c) The dependence of DP on the dipole moment, via quantum calculations. The dipole direction on the NPSG oligomer (DP = 4) was marked in red arrow. (d) The dielectric loss tangent (tan δ) of nanopolymer/SiO_2 bilayer at 500~10^5 Hz. (e) The transfer characteristics of top-gate/bottom-contact devices, where polystyrene (PS) and the doped NPSG serve as the dielectric layer; the pentacene serve as the semiconductor layer. The device structure is shown as well. (f) The field-effect carrier mobility (μ_{FET}) and the on/off ratio (I_{on}/I_{off}), extracted from (e).

polyfluorenes ($k \approx 2.75$) [33]. This feature is completely distinguished from the porous effect of covalent organic frameworks [34] that reduce k value to 1.2~1.6 through large free volume. Furthermore, compared with NPSG nanochains, SDG oligomers exhibit the relatively lower $k \approx 4.39$, suggesting that the covalently large-scale effect of NPSG can also be favorable to enhance polarization behaviors.

We further gain insight into the mechanism of polarization enhancement from the spiro-polygridization effect. Considering the frequency scope of 10^3~10^5 Hz, the high-k feature of NPSG likely originates from either electronic and atomic polarization or dipole polarization. In order to rule out electronic and atomic polarizations, we measured the optical dielectric constant (k_o). For NPSG film, the refractive index (n) of 1.66~1.81 and the extinction coefficient (K) of 0~0.008 are transformed into $k_o = 2.77 \sim 3.27$ at the high frequency of $3 \times 10^{14} \sim 7 \times 10^{14}$ Hz (Figure 3(b)), as comparable to SDG oligomers ($n = 1.77 \sim 1.66$ and $k_o = 2.74 \sim 3.13$) and PG-Cz ($n = 1.75 \sim 1.63$ and $k_o = 2.64 \sim 3.08$). The difference between k_o and k is obviously observed in polygrid backbones, especially for NPSG with $k - k_o = 5.16 \sim 5.66$. This feature is distinct from π-conjugated polyfluorenes ($n \approx 1.6$ and $k_o \approx 2.5$) [35] and polythiophenes ($n \approx 1.92$ and $k_o \approx 3.6$) [36] with $k \approx k_o$. Therefore, the high-k feature of NPSG nanochains is probably derived from the enhancement in dipole polarization.

The enhancement in dipole polarization was also confirmed by the theoretical calculations of dipole moment. In the NPSG oligomer models (Figure 3(c) and S69), we found that the dipole direction is roughly along the main-chain. Deeply, the dipole moment is gradually increased from 1.643 D (ungridized spiro-trimer), 1.919 D (SDG, DP = 2), 2.482 D (DP = 3) to 4.269 D (DP = 4). As a result, increasing the NPSG length enables to accumulate dipole moment. For longer NPSG nanochains, the ultralong persistence length allows the covalently ordered arrangement of STDF groups in rod-like main-chain conformation, versus coil-like backbones with disordered arrangements. In this case, such ultrarigid feature is favorable to maintain the dipole orientation (along the main-chain) and accumulatively enhance the dipole moment when increasing the DP. On this basis, the tiny pores of RG units (the sizes of 0.4 nm^2) on NPSG nanochains (even with few amount of structural defects, the electric properties were not influenced, see the following) suppress the effect of free volume on reducing the k value, which ensures the enhancement of dipole polarization in longer NPSG nanochains.

In addition, we examined the dielectric loss tangent (tan δ) of NPSG-containing films. In Figure 3(d), the NPSG/SiO$_2$ bilayer possesses tan $\delta = 0.05 \sim 0.20$ at $10^4 \sim 10^5$ Hz, which are obviously higher than that of the single SiO$_2$ layer with tan $\delta = 0.008 \sim 0.055$, the SDG/SiO$_2$ bilayer with tan $\delta = 0.02 \sim 0.08$, the PG-Cz/SiO$_2$ bilayer with tan $\delta = 0.006 \sim 0.027$, and polyfluorene/SiO$_2$ bilayer with tan $\delta = 0.01 \sim 0.03$ (Figure S70). These results suggest that adding NPSG layer obviously increases the leakage current and affords higher conductivity for dielectric layers [37], which is also consistent with the nature of higher dielectric constant.

We further fabricated pentacene OFETs by blending polystyrene- (PS-) based dielectric layer with NPSG to confirm the effect of high-k feature. Figure 3(e) exhibits the transfer characteristics when using the NPSG-doped dielectric layer. The SiO$_2$ layer is also used to maintain the low leakage current of OFET devices. Transistors with blending NPSG in the 1 : 10~1 : 5 ratio increase the drain current (I_{DS}) by 5 times in the saturation regimes at the negative gate voltage (V_{GS}) of -20~-25 V. Correspondingly, the field-effect mobility (μ_{FET}) of pentacene layer is obviously increased from $0.20 \pm 0.02\,\mathrm{cm}^2\ \mathrm{V}^{-1}\ \mathrm{s}^{-1}$ (undoped PS dielectric layer) to $0.90 \pm 0.04\,\mathrm{cm}^2\ \mathrm{V}^{-1}\ \mathrm{s}^{-1}$ (PS : NPSG = 10 : 1) and $0.82 \pm 0.08\,\mathrm{cm}^2\ \mathrm{V}^{-1}\ \mathrm{s}^{-1}$ (PS : NPSG = 5 : 1, Figure 3(f)), which are higher than $\mu_{FET} = 0.1 \sim 0.3\,\mathrm{cm}^2\ \mathrm{V}^{-1}\ \mathrm{s}^{-1}$ in common pentacene OFET devices [12, 38, 39]. Meanwhile, the on/off ratio (I_{on}/I_{off}) is increased from 3.57×10^4 (undoped PS layer) to 6.58×10^4 (NPSG-doping layer). Considering that the film morphology with larger roughness (Figure S71) should not enhance the carrier mobility, the high-k property of NPSG may be partly attributed to the improved OFET performances, because of the excellent screening effect on diminishing the interfacial coulomb impurities [39]. Further, doping high-k NPSG in the PS layer also results in the decreased threshold voltage from -5.37 V to -4.88~-4. 78 V, which is potential to develop OFET with lower operational voltage.

2.3. Excitonic Emission and Charge Carrier Transport in NPSG.

2.3. Excitonic Emission and Charge Carrier Transport in NPSG. To examine the effect of ultralong l_p feature and covalently large scale on the optoelectronic behaviors of NPSG (DP$_n \approx 26$), we also conducted a series of measurements such as ultraviolet-visual absorption (UV), photoluminescence (PL), carrier mobility, and single-molecular conductance.

For UV spectra in solution (Figure 4(a)), NPSG nanochains have an absorption peak at 343 nm and a wide shoulder peak at 368~370 nm. Although only with an efficient π -conjugation length on terfluorenes, NPSG possesses an optical bandgap (E_g) of ~3.11 eV, closely equivalent to that of tetrafluorenyl moieties (E_g = 3.10 eV) [32]. Moreover, even on π-interrupted backbones, E_g is still gradually decreased from 3.33 eV to 3.11 eV (Figure S72) when increasing the backbone length from ~2 nm (SDG) to >20 nm (NPSG). These results indicate that π-interrupted NPSG still benefits for the excitonic delocalization. For PL spectra in solution, NPSG shows a deep-blue emission at 415 nm with a lifetime of ~1.07 ns (Figure S73) and a larger Stokes shift of ~68 nm, totally different from ladder-type polymers [40] with small Stokes shifts of 5~25 nm. In the film state, NPSG still maintains a blue emission at ~430 nm without the obvious g-band defect emission, even after annealing under 260°C temperature at air atmosphere (Figure S74). Thus, NPSG-based wide-bandgap nanomaterials enable to compete with conjugated polyfluorenes [41], ZnO nanoparticles [42], and CNT (without emission) [43].

The carrier mobility of amorphous NPSG film (Figure S75) was investigated through the space-charge limited current (SCLC) method. Under the temperature of

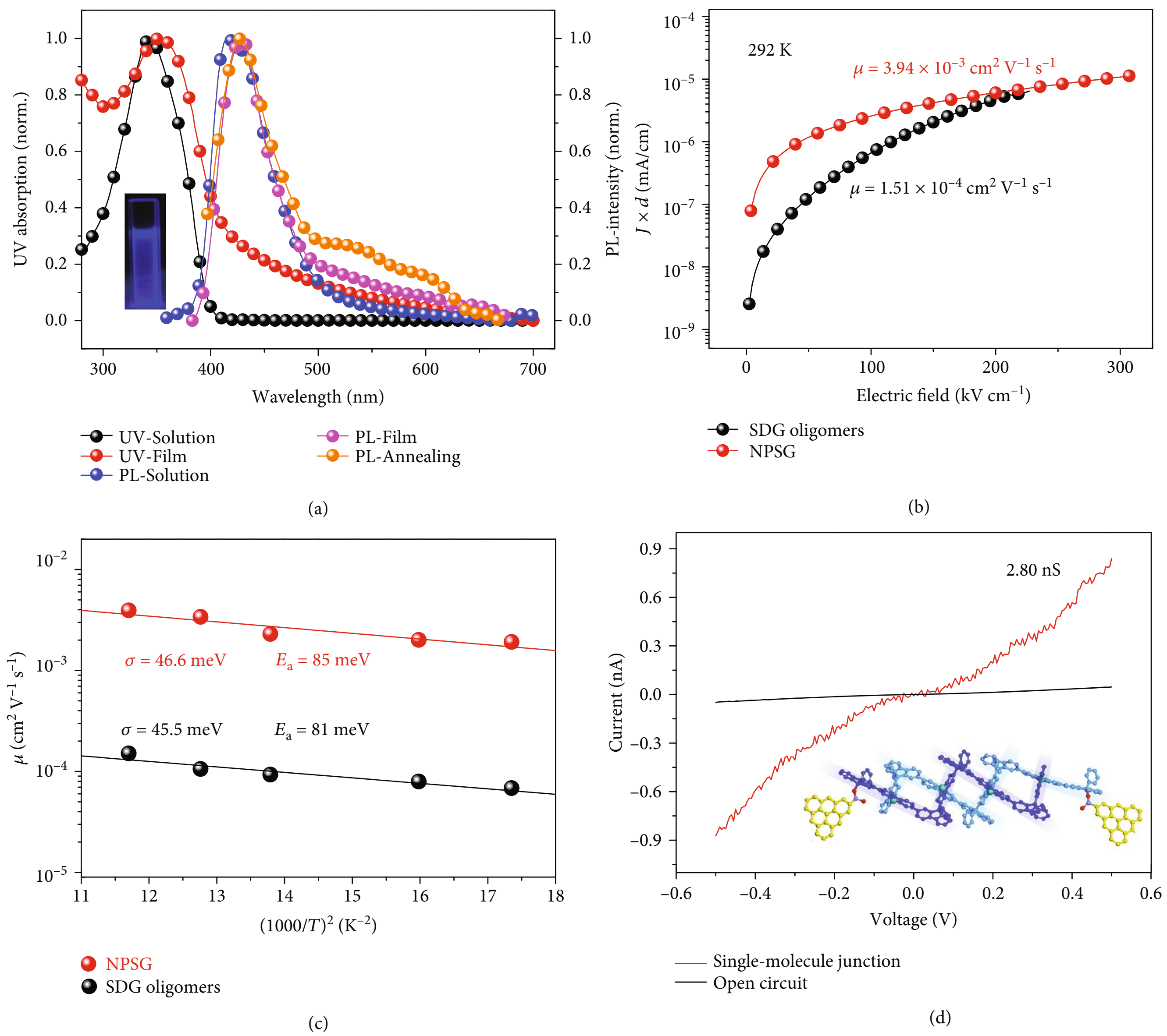

Figure 4: Optoelectronic features and carrier mobility of NPSG. (a) UV-vis absorbance and PL spectra of NPSG in solution ($CHCl_3$ solvent), pristine, and annealing film. (b) The space-charge limit current density (J) of NPSG (red) and SDG (black) at 292 K, along with their hole mobility. The d is the thickness of the film. (c) The dependence of temperature on hole mobility for NPSG (red) and SDG (black), along with the energy disorder (σ) and activation energy (E_a). (d) Current-voltage curves of single-chain NPSG and single-molecular devices.

292 K (Figure 4(b)), NPSG exhibits an outstanding zero-field hole mobility $\mu = 3.94 \times 10^{-3}$ cm^2 V^{-1} s^{-1}. To our best knowledge, such zero-field mobility is the highest value (Figure S77) among all fully π-interrupted molecules [44] with $\mu = 10^{-7} \sim 10^{-4}$ cm^2 V^{-1} s^{-1}. Particularly, it is unexpected that the zero-field hole mobility of π-interrupted NPSG can be even higher than that of amorphous π-conjugated polymers including polythiophenes [45] ($\mu \approx 1 \times 10^{-3}$ cm^2 V^{-1} s^{-1}) and polyfluorenes [46, 47] ($\mu \approx 10^{-7} \sim 10^{-4}$ cm^2 V^{-1} s^{-1}). In contrast, amorphous SDG oligomers exhibit an evidently lower current density under the same electric field and possess a lower mobility $\mu = 1.51 \times 10^{-4}$ cm^2 V^{-1} s^{-1}, as an order of magnitude lower than that of NPSG. In addition, versus NPSG, the SCLC curve of SDG shows a stronger electric-field-dependent feature in current density (Figure S79), which suggests the presence of more deep-traps [48]. These results support the effect of covalently large scale on improving charge transport, which was ever hidden by the effective π-conjugation length and was diminished by the short persistence length in conventional organic semiconductors [15].

Further, we studied the energy disorder and activation energy of amorphous NPSG film to uncover the physical mechanism during carrier transport. In Figure 4(c), even under low temperature at 240 K, NPSG still displays a high carrier mobility of $\mu = 1.93 \times 10^{-3}$ cm^2 V^{-1} s^{-1} and shows a relatively weak temperature dependence on hole transport. According to the Gaussian disorder model [*49*], NPSG displays an ultralow energy disorder (σ) of 46.6 meV, which is far lower than that of amorphous π-conjugated polymers (Figure S81) with obviously shorter l_p, including polyfluorenes [*46*] with $\sigma \approx 100$ meV and $l_p \approx 6 \sim 9$ nm, poly-*p*-phenylene vinylenes [*50*] with $\sigma \approx 160$ meV and $l_p \approx 7$ nm, and polythiophenes [*45*, *49*] with $\sigma \approx 70$ meV and $l_p \approx 3 \sim 10$ nm. Meanwhile, the activation energy (E_a) of amorphous NPSG film is 85 meV that can even fall into the semicrystalline range [*7*] of polythiophenes with $E_a = 50 \sim 100$ meV, as lower than other amorphous conjugated polymers [*7*] with $E_a = 150 \sim 250$ meV. These results confirm the ultralong persistence length effect that efficiently suppresses the defect scattering and trapping levels to decrease the width of density-of-states (DOS). Deeply, through quantum calculation (Figures S82-S84), the highest occupied molecular orbital (HOMO) and its degenerated orbital levels for hole transport are distributed on both dithiophenyl and monofluorenyl planes of STDF moieties, which are arranged in covalently well-ordered states for the narrow DOS feature. In addition, the ultralow energy disorder is similarly observed in SDG oligomers ($\sigma = 45.5$ meV and $E_a = 81$ meV). These results reveal that even with structural defects in low amount (such as ungridized or branching defects that can increase conformational entropy), the electric properties of our synthesized NPSG nanochains are not influenced obviously. Moreover, the above ultralow σ level confirms the theoretical observation of gridization effect on lowering reorganization energy [*51*]. Notably, the ultralow energy disorder can be integrated with high-k feature perfectly, which cannot be possible in other high-k organic polymers via adding polar groups on flexible alkyl chains [*52*]. High-k-based NPSG with ultralow energy disorder offers a potential approach to design advanced donor/acceptor materials in the application of OPVs.

Single-molecular diode was also applied to investigate the effect of π-interrupted NPSG backbone on the single-chain conductance (G). The NPSG single-chain (with the length of 15~20 nm) was covalently linked by graphene segments (as the electrodes), and then, the voltage between two graphene segments was applied to obtain the current (I)-voltage (V) curve. Generally, the conjugated planar polymer such as polyporphyrin nanochains exhibits the relatively high conductance $G = 10^2 \sim 10^4$ nS [*17*]. In contrast, NPSG single-chain exhibits the highest conductance up to $G = 2.8$ nS (in Figure 4(d)), which is at least two orders of magnitude lower than that of conjugated polymer chains. This result is consistent with the feature of π-interrupted main-chain that disfavors the π-electronic delocalization and transport behaviors. Even so, the I-V curve of NPSG single-chain exhibits the approximately symmetric pattern where the conductance is enhanced with increasing the bias from 0 to 0.5 V, reflecting the feature of typically molecular diode. Thus, NPSG nanochains would be favorable for the semiconducting molecular nanowires or nanoelectronics.

3. Conclusion

In summary, a state-of-the-art ultrarigid spiro-nanopolymer has been created to explore the effect of covalent nanoscale ordering on the ultralow energy disorder and high dielectric constant. Conformational entropy has been effectively suppressed by spiro-polygridization to achieve the recording rigidity with $l_p \approx 41$ nm. As a result, the dipole polarization is enhanced by large covalent nanoscale effect to give the higher dielectric constant ($k = 8.43$), as approximate to GaN ($k \approx 9$). Furthermore, conformational defects and trapping levels are reduced, which gives an excellent hole mobility ($\mu = 3.94 \times 10^{-3}$ cm^2 V^{-1} s^{-1}). To our best knowledge, these results surpass all amorphous π-conjugated polymer semiconductors reported in the literatures. Our polygridization strategy probably become the powerful cross-scale chemistry to hierarchically modulate the nature of organic nanopolymers that would open a new door to challenge the physical optoelectronic extreme and to make recording performance of semiconducting device. By means of such polygridization-type molecular integration technology (MIT), organic nanopolymer semiconductors would become potential candidates of the fourth-generation semiconductors with the feature of high-performance, multifunctionality, intelligence, and ubiquity to fulfill the requirement of flexible electronics, nanoelectronics, and organic intelligence.

4. Materials and Methods

4.1. Materials. The detailed synthetic procedures of substrate synthons and NPSG chains are described in the Supplementary Information files.

4.2. Gel Permeation Chromatography (GPC). The GPC characteristics were conducted on a HP1100 HPLC system possessing 7911GP-502 and GPC columns using polystyrenes as the standard and tetrahydrofuran (THF) as the eluent at a flow rate of 1.0 ml/min at 25°C. The concentrations of NPSG solutions were about 0.8 mg/ml.

4.3. Dynamic Light Scattering (DLS) and Static Light Scattering (SLS). The DLS characterizations of NPSG solution ($CHCl_3$ as a solvent) were determined by a Brookhaven Instrument (ZetaPALS) to obtain R_h. The operating wavelength of light source is 632.8 nm. The SLS measurements were performed to calculate R_g, via ALV/CGS-3 light-scattering spectrometer that is equipped with an ALV/LSE-7004 multiple-τ digital correlator. All of the operating wavelength are 632.8 nm for light source.

4.4. Small-Angel X-Ray Scattering (SAXS). The scattering datum was provided via the synchrotron radiation SAXS from Shanghai Synchrotron Radiation Facility. The distance from the sample cell (with mica windows in the path length of 1.5 mm) to the detector is 1 m. The wavelength of X-ray is 1.2 Å. The collected scattering vectors q ranges from 0.01 to 0.4 nm^{-1}. The substrate of the solvent (toluene) from the solution scattering was performed before the analysis. The data were collected with the exposure time of 2 s, the acquired period of 2.01 s, and the images of 10. The measured NPSG solutions were 0.5~2 mg/ml in toluene solvents.

4.5. Molecular Dynamic Simulations. The molecular models of NPSG-based spirotrigrids were constructed and calculated via the Forcite plus module in the software Materials Studio. The geometry optimization was performed based on the SMART algorithm (as the cascade Steepest Descent-ABNR-Quasi-Newton algorithm). The simulations of conformational motions of spirotrigrids were based on the NVT ensemble (in vacuum), the pcff forcefield, the timestep of 0.2 fs, and the total time of 100 ps.

4.6. The Calculation of Dielectric Constant (k) of NPSG. The diode device structure Cu/SiO_2/NPSG/Si (n^+) was fabricated to measure the total capacitance C_i, which is transformed to k via the equation $\varepsilon_0/C_i = d_s/k_s - d/k$, where d_s, k_s, and ε_0 are defined as the layer thickness, the dielectric constant of SiO_2 ($k_s = 4.0$) [9], and the permittivity of vacuum (8.85×10^{-12} F/m), respectively. The NPSG layer (from the DCE solution with the NPSG concentration of 5 mg/ml) was spin-coated on the SiO_2 layer, which was followed by annealing under the conditions of a vacuum environment, 80°C and 30 min. The procedure and conditions of spin-coating other polymers/oligomer films were the same as those of NPSG. C_i was measured via an impedance analyzer (IM3533), through a frequency sweep of 500~100000 Hz and a bias of 0.1 V. The thicknesses of the NPSG film were measured by ellipsometry (J.A. Woollam RC2). The dielectric loss (tan δ) of NPSG-based diode device (bilayer of NPSG and SiO_2) was afforded via impedance analyzer at 10^3~10^5 Hz. The optical dielectric constant (k_o) of NPSG, in the high-frequency range of $3 \times 10^{14} \sim 8 \times 10^{14}$ Hz, was calculated via the equation $k_o = n^2 - K^2$, where n and K are defined as the refractive index and the extinction coefficient, respectively. Both were afforded via the ellipsometry characterization.

4.7. OFET Device. We used a heavily doped n-type Si wafer (as the control gate) containing a 50 nm-thick SiO_2 layer, which serves as the control dielectric layer. The surface of Si wafer is carefully washed by acetone, ethanol, and deionized water in 20 minutes, via ultrasonic cleaning, which is followed by blowing with nitrogen atmosphere. Then, these wafers were dried over in the vacuum atmosphere (under the temperature of 120°C and 30 minutes). The polystyrene or the mixed polystyrene and NPSG samples were dissolved in 1,2-dichloroethane and then spin coated on SiO_2 as a polymer dielectric layer. The semiconductor layer of 50 nm thick pentacene was deposited onto the PS layer or mixed PS and NPSG layer, under the thermal vacuum evaporation method at 5×10^4 Pa. The Cu film with the thickness of 100 nm, serving as the source and drain electrodes, was thermally evaporated through a shadow mask. The channel length (L) and width (W) were 150 and 1500 μm, respectively. All of the devices were synchronously fabricated at the same conditions and characterized in a shielding box in ambient air (RH = 2%), using a Keithley 2636B semiconductor parameter analyzer.

4.8. Ultraviolet-Visual Absorption (UV-vis) and Photoluminescence Spectra (PL). The solution was prepared under the concentration of 10^{-2} mg/ml in $CHCl_3$ or DCE solvent. The film was spin-coated from the solution (DCE solvent, the concentration of 8 mg/ml) under the 800 rad/s. The UV spectra (LAMBDA 35) were used to characterize the photophysical properties of their ground states. The PL spectra (RF-6000 Plus) were obtained to study the excitonic behaviors of their excited states.

4.9. Measurement of Space-Charged-Limited Current for Carrier Mobility. The hole-only device with the structure of ITO/PEDOT:PSS/NPSG/Au was fabricated according to the literature [49]. The poly(3,4-ethylenedioxythiophene)-doped poly(styrene sulfonic acid) (PEDOT : PSS) layer and NPSG layer (or SDG oligomers, both in chlorobenzene solvent) were prepared via spin-coating at the spin rate 7000 RPM and annealing under 140°C (10 min). For the space-charged-limited current measurement, injecting the charge carriers into the thin-film active layer was performed under the DC voltage, through a source measure unit (SMU) Keithley (Model 2612B) that also records the currents under different voltage conditions. The calculation of zero-field carrier mobility is based on the $J \sim E^2$ region in the SCLC curve (where J and E are the current density and electric field, respectively) to ensure the low deviation.

4.10. Single-Molecular Electronic Device. A new dash-line lithographic (DLL) method, referred to the literature [53], was used to fabricate the single-molecular electronic device. For the linkage of a polymeric single-chain via ester linkage, NPSG were dissolved in dichloromethane with the concentration ~10^{-4} M, followed by adding graphene devices and carbodiimide dehydrating/activating agent. After 2 days, the NPSG device was taken out from solution. Such device was washed through copious acetone and ultrapure water solvent and then was dried under N_2 atmosphere. We used an Agilent 4155C semiconductor characterization system and a Karl Suss (PM5) manual probe station to measure the current (I)-voltage (V) curve under the ambient atmosphere.

Data Availability

All data is available in the main text or the Supplementary Information. The data are available from the corresponding author on reasonable request.

Conflicts of Interest

The authors declare no competing interests.

Authors' Contributions

Dongqing Lin has written this manuscript and Supplementary Materials, performed polygridization, simulated conformational relaxations, investigated the single-chain properties, and analyzed all datum. Wenhua Zhang has provided SAXS characterizations. Yang Li, Yongxia Yan, Hongkai Hu, and Lei Tang have synthesized the substrates of NPSG. Hang Yin and Haixia Hu have measured and calculated the carrier mobility. Haifeng Ling and Le Wang have measured and calculated the dielectric constant. Xinmiao Xie and Xuefeng Guo have fabricated the single-molecular electronic device to measure the conductance of NPSG. Dan Lu and Hao Zhang have provided SLS characterizations. Ying Wei has provided significant suggestions on the synthesis of NPSG and carefully checked this manuscript and Supplementary Materials. Zhang He, Shasha Wang, Jin'an Liu, and Yue Qian have provided crucial help in nanotechnological and photophysical characterizations. Yongxia Wang and Chaoyang Dong have helped to address the figures in Figure 1 (NPSG models). Linghai Xie and Wei Huang have initiated this project, provided crucial idea, and offered enough funds for this work.

Acknowledgments

We thank Shanghai Synchrotron Radiation Facility (SSRF) for providing synchrotron radiation SAXS instruments (BL19U2). We thank Daxia Xia and Haowan Cheng from Shiyanjia Lab (http://www.Shiyanjia.com) for the simulation of the vibrational modes and the molecular orbital distribution, as well as providing the ellipsometry and MS measurements. This work was supported by the National Natural Science Foundation of China (21774061, 22071112, and 61935017), National Key Laboratory (2009DS690095), Natural Science Foundation Major Research Program Integration Project (Grant Number 91833306), Natural Science Fund for Colleges and Universities in Jiangsu Province (20KJB150038), and Open Project from State Key Laboratory of Supramolecular Structure and Materials at Jilin University (No. sklssm202014 and sklssm202108).

Supplementary Materials

Figure S1: synthetic routes of NPSG. Figure S2: the nanoarchitectures of rhombus-type grids (RGs) and single-bond-linked polygrids (SBPGs). Figure S3: the diastereoisomers of RGs. Figure S4: the nanoarchitectures of spirodigrids (SDGs), and single-bond-linked rhombus-type digrids (SRDGs). Figure S5: the diastereoisomers of SDG. Figure S6: the NPSG chains with various tacticity and interlaced or uninterlaced types. Figure S7: the helical backbones of SS-isotactic and RR-isotacticity NPSG backbones (all in interlaced states). Figure S8: the retrosynthetic analysis of NPSG. Figure S9: the geometric matching model of STF-DOH intermediates (carbon cationic species). Figure S10: the reaction time (t_r) dependence of polygridization. Figure S11: the likely structure of hyperbranched polymer (HBPG) from the spiro-polygridization. Figure S12: the $C_{\text{STF-DOH}}$ dependence of polygridization. Figure S13: the GPC spectra of spirodigrids (a) and the oligomers of NPSG (b). Table S1: the relationship between elution time and molar mass of NPSG oligomers. Table S2: the elution time of NPSG with individual molar mass (extrapolated via its calibration equation). Figures S14, S15, S16, S17, S18, S19, S20, S21, S22, S23, S24, S25, and S26: the GPC spectra of NPSG. Figures S27 and S28: the hydrodynamic radius (R_h) of NPSG. Figure S29: MS spectra of SDG (a) and spirotrigrid (b). Figure S30: MS spectra simulation of ungridized defective SDG structures. Figure S31: MS spectra simulation of ungridized defective spriotrigrid structures. Figure S32: MS spectra of NPSG oligomers. Figure S33: ^{13}C NMR spectra of STF-DOH, STF-DOH-2H (dehydroxylated STF-DOH, as the byproduct) SDG, and NPSG. Figure S34: FT-IR spectra of NPSG. Figure S35: the relationship between Mark-Houwink exponent α and persistence length (in θ or stretched state). Figure S36: the hydrodynamic radius models of the NPSG chain ($\text{DP} = 8$ as an example). Figure S37: the NPSG single-chain image from atomic force microscopy (AFM), with the height profiles (in blue region). Figure S38: the Kratky plots of NPSG (not green lines) and BSG (green lines, in the green region of branch with chain folding) in toluene. Figure S39: the special mass fractal dimension of NPSG and other polymers. Figure S40: the distance distribution function $P(r)$ of NPSG with various average chain lengths. Figure S41: the distance distribution function $P(r)$ of HBPG. Figures S42, S43, and S44: the radius of gyration of NPSG with various contour lengths. Figure S45: the radius of gyration of HBPG with average chain length $L \approx 52.2\,\text{nm}$ (transformed from R_h values). Figure S46: the NPSG position (marked in red stars) in the statistical graph of persistence length and monomeric sizes. Figure S47: the models of calculating persistence length. Figures S48, S49, S50, S51, S52, S53, S54, S55, and S56: the conformational relaxations of spirotrigrids and STRG with various tacticies. Figure S57: the conformational relaxation of single-stranded ungridized oligomers whose polymers originate from the deletion of the spiro-carbon atoms on NPSG backbones (SSIP). Figure S58: the ungridized defective NPSG oligomer model. Figures S59 and S60: the conformational relaxations of ungridized defective spirotrigrids with various tacticities. Figures S61, S62, S63, and S64: the capacity of SiO_2 layer, NPSG-based diode device, SDG oligomer-based diode device, and PG-Cz-based diode device, respectively. Figures S65, S66, and S67: the refractive index (n) and the extinction coefficient (K) of NPSG, SDG, and PG-Cz, respectively, in the wavelength range of 300~1000 nm. Figure S68: the optical dielectric constant (k_o) of NPSG, SDG oligomers, and PG-Cz in the high-frequency range of $3 \times 10^{14} \sim 1 \times 10^{15}$ Hz. Figure S69: the direction of dipole moment (marked in blue lines) of spiro-trimer, SDG, spiro-trimer, and spirotetramer. Figure S70: the dielectric loss tangent ($\tan \delta$) of polyfluorene/SiO_2 bilayer. Figure S71: AFM image of polystyrene (PS) and polystyrene-NPSG doping films. Table S3: the photophysical parameters of NPSG solutions. Figure S72: UV-PL spectra of STF-DOH and NPSG (in $CHCl_3$ solvent) with various DP_n. Figure S73: transition decay and lifetimes of NPSG in $CHCl_3$ solvent. Figure S74: photophysical properties of STF-DOH, SDG, and NPSG. Table S4: the photophysical parameters of NPSG film (spin-coated from DCE solution). Figure S75: the X-ray diffraction (XRD) of spin-coated NPSG film. Figure S76: the DSC characterization of NPSG. Figure S77: the zero-field carrier mobility of various organic small molecules and polymers in amorphous state. Figure S78: the dependence of space-charged-limited current density $(J) \times$ (film thickness of NPSG/SDG) d on the electric field, under the temperature of 240 K. Figures S79 and S80: fitting of SCLC curve of NPSG and SDG under the temperature of 293 K and 240 K, respectively. Figure S81: the energy disorder of various organic small molecules and polymers in amorphous state. Figures S82, S83, and S84: the molecular orbital distribution of SDG, spirotrigrid, and spirotetragrid, respectively. Figure S85: a macroscopic pattern of NPSG-based molecular electronic device. Figure S86: the SEM imagine of molecular electronic device. Figures S87, S88, S89, S90, S91, S92, S93, S94, S95, S96, S97, and S98: ^{1}H and ^{13}C NMR spectra of substrates, intermediates, and NPSGs. *(Supplementary Materials)*

References

[1] L. H. Xie, C. R. Yin, W. Y. Lai, Q. L. Fan, and W. Huang, "Polyfluorene-based semiconductors combined with various periodic table elements for organic electronics," *Progress in Polymer Science*, vol. 37, no. 9, pp. 1192–1264, 2012.

[2] X. M. Xie, Y. Wei, D. Q. Lin, C. Zhong, L. Xie, and W. Huang, "Nanogridarene: a rising nanomolecular integration platform of organic intelligence," *Chinese Journal of Chemistry*, vol. 38, no. 1, pp. 103–105, 2020.

[3] H. Bronstein, C. B. Nielsen, B. C. Schroeder, and I. McCulloch, "The role of chemical design in the performance of organic semiconductors," *Nature Reviews Chemistry*, vol. 4, no. 2, pp. 66–77, 2020.

[4] T. L. Wu, M. J. Huang, C. C. Lin et al., "Diboron compound-based organic light-emitting diodes with high efficiency and reduced efficiency roll-off," *Nature Photonics*, vol. 12, no. 4, pp. 235–240, 2018.

[5] L. X. Meng, Y. M. Zhang, X. J. Wan et al., "Organic and solution-processed tandem solar cells with 17.3% efficiency," *Science*, vol. 361, no. 6407, pp. 1094–1098, 2018.

[6] J. G. Mei, Y. Diao, A. L. Appleton, L. Fang, and Z. Bao, "Integrated materials design of organic semiconductors for field-effect transistors," *Journal of the American Chemical Society*, vol. 135, no. 18, pp. 6724–6746, 2013.

[7] R. Noriega, J. Rivnay, K. Vandewal et al., "A general relationship between disorder, aggregation and charge transport in conjugated polymers," *Nature Materials*, vol. 12, no. 11, pp. 1038–1044, 2013.

[8] M. A. Green, A. Ho-Baillie, and H. J. Snaith, "The emergence of perovskite solar cells," *Nature Photonics*, vol. 8, no. 7, pp. 506–514, 2014.

[9] C. L. Wang, Z. B. Zhang, S. Pejić et al., "High dielectric constant semiconducting poly (3-alkylthiophene) s from side chain modification with polar sulfinyl and sulfonyl groups," *Macromolecules*, vol. 51, no. 22, pp. 9368–9381, 2018.

[10] L. Zhu, "Exploring strategies for high dielectric constant and low loss polymer dielectrics," *Journal of Physical Chemistry Letters*, vol. 5, no. 21, pp. 3677–3687, 2014.

[11] J. Brebels, J. V. Manca, L. Lutsen, D. Vanderzande, and W. Maes, "High dielectric constant conjugated materials for organic photovoltaics," *Journal of Materials Chemistry A*, vol. 5, no. 46, pp. 24037–24050, 2017.

[12] Y. X. Wang, X. Y. Huang, T. Li, L. Li, X. Guo, and P. Jiang, "Polymer-based gate dielectrics for organic field-effect transistors," *Chemistry of Materials*, vol. 31, no. 7, pp. 2212–2240, 2019.

[13] Z. H. Zhu, Y. L. Guo, and Y. Q. Liu, "Application of organic field-effect transistors in memory," *Materials Chemistry Frontiers*, vol. 4, no. 10, pp. 2845–2862, 2020.

[14] S. Wang, P. J. Chia, L. L. Chua et al., "Band-like transport in surface-functionalized highly solution-processable graphene nanosheets," *Advanced Materials*, vol. 20, no. 18, pp. 3440–3446, 2008.

[15] G. D. Scholes and G. Rumbles, "Excitons in nanoscale systems," *Nature Materials*, vol. 5, no. 9, pp. 683–696, 2006.

[16] H. M. Heitzer, T. J. Marks, and M. A. Ratner, "Computation of dielectric response in molecular solids for high capacitance organic dielectrics," *Accounts of Chemical Research*, vol. 49, no. 9, pp. 1614–1623, 2016.

[17] G. Sedghi, L. J. Esdaile, H. L. Anderson et al., "Comparison of the conductance of three types of porphyrin-based molecular wires: β, meso, β-fused tapes, meso-butadiyne-linked and twisted meso-meso linked oligomers," *Advanced Materials*, vol. 24, no. 5, pp. 653–657, 2012.

[18] T. Ikai, T. Yoshida, K. Shinohara, T. Taniguchi, Y. Wada, and T. M. Swager, "Triptycene-based ladder polymers with one-handed helical geometry," *Journal of the American Chemical Society*, vol. 141, no. 11, pp. 4696–4703, 2019.

[19] P. Ruffieux, S. Y. Wang, B. Yang et al., "On-surface synthesis of graphene nanoribbons with zigzag edge topology," *Nature*, vol. 531, no. 7595, pp. 489–492, 2016.

[20] C. L. Gettinger, A. J. Heeger, J. M. Drake, and D. J. Pine, "A photoluminescence study of poly (phenylene vinylene) derivatives: the effect of intrinsic persistence length," *Journal of Chemical Physics*, vol. 101, no. 2, pp. 1673–1678, 1994.

[21] D. Q. Lin, Y. Wei, A. Z. Peng et al., "Stereoselective gridization and polygridization with centrosymmetric molecular packing," *Nature Communications*, vol. 11, no. 1, pp. 1756–1766, 2020.

[22] L. Wang, G.-W. Zhang, C.-J. Ou et al., "Friedel–Crafts bottom-up synthesis of fluorene-based soluble luminescent organic nanogrids," *Organic Letters*, vol. 16, no. 6, pp. 1748–1751, 2014.

[23] Y. Wei, M. Luo, G. Zhang, J. Lei, L.-H. Xie, and W. Huang, "A convenient one-pot nanosynthesis of a C(sp2)–C(sp3)-linked 3D gridviaan 'A2+ B3' approach," *Organic & Biomolecular Chemistry*, vol. 17, no. 27, pp. 6574–6579, 2019.

[24] L. H. Xie, X. Y. Hou, Y. R. Hua et al., "Facile synthesis of complicated 9,9-diarylfluorenes based on $BF_3 \cdot Et_2O$-mediated Friedel–Crafts reaction," *Organic Letters*, vol. 8, no. 17, pp. 3701–3704, 2006.

[25] M. Nagai, J. Huang, T. D. Zhou, and W. Huang, "Effect of molecular weight on conformational characteristics of poly (3-hexyl thiophene)," *Journal of Polymer Science Part B: Polymer Physics*, vol. 55, no. 17, pp. 1273–1277, 2017.

[26] M. Jikei and M. Kakimoto, "Hyperbranched polymers: a promising new class of materials," *Progress in Polymer Science*, vol. 26, no. 8, pp. 1233–1285, 2001.

[27] T. J. Prosa, B. J. Bauer, and E. J. Amis, "From stars to spheres: a SAXS analysis of dilute dendrimer solutions," *Macromolecules*, vol. 34, no. 14, pp. 4897–4906, 2001.

[28] H. D. T. Mertens and D. I. Svergun, "Structural characterization of proteins and complexes using small-angle X-ray solution scattering," *Journal of Structural Biology*, vol. 172, no. 1, pp. 128–141, 2010.

[29] P. M. Cotts, T. M. Swager, and Q. Zhou, "Equilibrium flexibility of a rigid linear conjugated polymer," *Macromolecules*, vol. 29, no. 23, pp. 7323–7328, 1996.

[30] J. H. Chen, C. S. Chang, Y. X. Chang, C. Y. Chen, H. L. Chen, and S. A. Chen, "Gelation and its effect on the photophysical behavior of poly (9,9-dioctylfluorene-2,7-diyl) in toluene," *Macromolecules*, vol. 42, no. 4, pp. 1306–1314, 2009.

[31] C. Bustamante, J. F. Marko, E. D. Siggia, and S. Smith, "Entropic elasticity of lambda-phage DNA," *Science*, vol. 265, no. 5178, pp. 1599-1600, 1994.

[32] Q. Y. Feng, Y. L. Han, M. N. Yu et al., "A robust and soluble nanopolymer based on molecular grid-based nanomonomer," *Chinese Journal of Polymer Science*, vol. 35, no. 1, pp. 87–97, 2017.

[33] J. J. Wang, K. Li, C. Yuan et al., "Variable polymer properties driven by substituent groups: investigation on a trifluorovinylether-functionalized polyfluorene at the C-9 position," *Macromolecular Chemistry and Physics*, vol. 216, no. 7, pp. 742–748, 2015.

[34] P. P. Shao, J. Li, F. Chen et al., "Flexible films of covalent organic frameworks with ultralow dielectric constants under high humidity," *Angewandte Chemie International Edition*, vol. 57, no. 50, pp. 16501–16505, 2018.

[35] P. O. Morawska, Y. Wang, A. Ruseckas et al., "Side-chain influence on the mass density and refractive index of polyfluorenes and star-shaped oligofluorene truxenes," *Journal of Physical Chemistry C*, vol. 119, no. 38, pp. 22102–22107, 2015.

[36] P. Boufflet, G. Bovo, L. Occhi et al., "The influence of backbone fluorination on the dielectric constant of conjugated polythiophenes," *Advanced Electronic Materials*, vol. 4, no. 10, article 1700375, 2018.

[37] L. L. Sun, B. Li, Y. Zhao, G. Mitchell, and W. H. Zhong, "Structure-induced high dielectric constant and low loss of CNF/PVDF composites with heterogeneous CNF distribution," *Nanotechnology*, vol. 21, no. 30, article 305702, 2010.

[38] H. F. Ling, J. Y. Lin, M. D. Yi et al., "Synergistic effects of self-doped nanostructures as charge trapping elements in organic field effect transistor memory," *ACS Applied Materials & Interfaces*, vol. 8, no. 29, pp. 18969–18977, 2016.

[39] Z. B. Zhang, J. F. Zheng, K. Premasiri et al., "High-κ polymers of intrinsic microporosity: a new class of high temperature and low loss dielectrics for printed electronics," *Materials Horizons*, vol. 7, no. 2, pp. 592–597, 2020.

[40] F. Trilling, M. K. Ausländer, and U. Scherf, "Ladder-type polymers and ladder-type polyelectrolytes with on-chain dibenz[a,h]anthracene chromophores," *Macromolecules*, vol. 52, no. 8, pp. 3115–3122, 2019.

[41] U. Scherf and E. J. W. List, "Semiconducting polyfluorenes—towards reliable structure–property relationships," *Advanced Materials*, vol. 14, no. 7, pp. 477–487, 2002.

[42] C. Ton-That, L. Weston, and M. R. Phillips, "Characteristics of point defects in the green luminescence from Zn- and O-rich ZnO," *Physical Review B*, vol. 86, no. 11, article 115205, 2012.

[43] M. J. O'Connell, S. M. Bachilo, C. B. Huffman et al., "Band gap fluorescence from individual single-walled carbon nanotubes," *Science*, vol. 297, no. 5581, pp. 593–596, 2002.

[44] D. P. Tabor, V. A. Chiykowski, P. Friederich et al., "Design rules for high mobility xanthene-based hole transport materials," *Chemical Science*, vol. 10, no. 36, pp. 8360–8366, 2019.

[45] A. J. Mozer, N. S. Sariciftci, A. Pivrikas et al., "Charge carrier mobility in regioregular poly(3-hexylthiophene) probed by transient conductivity techniques: a comparative study," *Physical Review B*, vol. 71, no. 3, article 035214, 2005.

[46] J. C. Blakesley, H. S. Clubb, and N. C. Greenham, "Temperature-dependent electron and hole transport in disordered semiconducting polymers: analysis of energetic disorder," *Physical Review B*, vol. 81, no. 4, article 045210, 2010.

[47] C. C. Wu, T. L. Liu, W. Y. Hung et al., "Unusual nondispersive ambipolar carrier transport and high electron mobility in amorphous ter(9,9-diarylfluorene)s," *Journal of the American Chemical Society*, vol. 125, no. 13, pp. 3710-3711, 2003.

[48] V. R. Nikitenko, H. Heil, and H. von Seggern, "Space-charge limited current in regioregular poly-3-hexyl-thiophene," *Journal of Applied Physics*, vol. 94, no. 4, pp. 2480–2485, 2003.

[49] H. Yin, S. H. Cheung, J. H. L. Ngai et al., "Thick-film high-performance bulk-heterojunction solar cells retaining 90% PCEs of the optimized thin film cells," *Advanced Electronic Materials*, vol. 3, no. 4, article 1700007, 2017.

[50] D. Abbaszadeh, A. Kunz, G. A. H. Wetzelaer et al., "Elimination of charge carrier trapping in diluted semiconductors," *Nature Materials*, vol. 15, no. 6, pp. 628–633, 2016.

[51] L. Yang, J. Mao, C. Z. Yin et al., "A novel structure of grid spirofluorene: a new organic semiconductor with low reorganization energy," *New Journal of Chemistry*, vol. 43, no. 20, pp. 7790–7796, 2019.

[52] B. Xu, X. P. Yi, T. Y. Huang et al., "Donor conjugated polymers with polar side chain groups: the role of Dielectric constant and energetic disorder on photovoltaic performance," *Advanced Functional Materials*, vol. 28, no. 46, article 1803418, 2018.

[53] C. C. Jia, J. Y. Wang, C. J. Yao et al., "Conductance switching and mechanisms in single-molecule junctions," *Angewandte Chemie International Edition*, vol. 52, no. 33, pp. 8666–8670, 2013.